

Lidar-based minute-scale offshore wind speed forecasts analysed under different atmospheric conditions

FRAUKE THEUER^{1*}, MARIJN FLORIS VAN DOOREN¹, LUEDER VON BREMEN² and MARTIN KÜHN¹

¹ForWind, Institute of Physics, University of Oldenburg, Germany

²German Aerospace Center (DLR) – Institute of Networked Energy Systems, Oldenburg, Germany

(Manuscript received April 1, 2021; in revised form September 16, 2021; accepted September 23, 2021)

Abstract

In recent years, the potential of remote sensing-based minute-scale forecasts to improve the integration of wind power into our energy system has been shown. In lidar-based forecasts, the wind speed is extrapolated from the measuring to the forecast height, i.e. the wind turbines' hub height, by assuming a stability-corrected logarithmic wind profile. The objective of this paper is the significant reduction of large forecasting errors associated with the height extrapolation. Hence, we introduce two new approaches and characterise their skill under different atmospheric conditions. The first one is based on an empirical set of parameters derived from lidar data and operational wind turbine data. The second approach derives the wind speed tendency of two consecutive forecasts at the measuring height and applies this to operational wind speed data at hub height. We identified the uncertainty in stability estimates and measurement height as the main cause for large extrapolation errors of the existing lidar-based forecast. Monte Carlo simulations revealed the new approaches' low sensitivity to uncertainty in lidar data processing, propagation and height extrapolation. Forecasting errors of a 5-minute-ahead wind speed forecast of free flow turbines at an offshore wind farm were significantly reduced for the two newly developed methods as compared to the existing forecast during stable atmospheric conditions. Persistence could be outperformed during unstable and neutral atmospheric conditions and for situations with higher turbulence intensity. Overall, we found lidar-based forecasts to be less sensitive to atmospheric conditions than persistence. We discuss the importance of accurate vertical wind speed profile estimation, the advantages and shortcomings of the two newly introduced methods and their skill compared to persistence. In conclusion, the additional use of wind turbine operational data can significantly improve minute-scale lidar-based forecasts. We further conclude that the characterisation of forecast skill dependent on atmospheric conditions can be valuable for decision-making processes.

Keywords: atmospheric stability, remote sensing, turbine operational data, uncertainty assessment, very short-term forecast, wind energy

1 Introduction

The increasing penetration of renewable energies in our power system causes a growing demand for skilful minute-scale wind speed and power forecasts (WÜRTH et al., 2019). Such forecasts can be valuable tools for both the physical balancing, i.e. assuring grid stability, reducing curtailment and providing reserve power (LIANG et al., 2016), as well as the economic balancing of power, i.e. for trading purposes (CALI, 2011). A variety of minute-scale forecasting methods has been investigated in the course of many years, including time series models such as persistence, ARMA (autoregressive moving average) and ARIMA (autoregressive integrated moving average) models (WÜRTH et al., 2019; TORRES et al., 2005), machine learning approaches and neural networks (GENDEEL et al., 2018), spatio-temporal models (LENZI et al., 2018), as well as hybrid approaches (ZHOU et al., 2018). In recent years the potential of remote sensing measurements for minute-scale forecasts

has been shown. In particular, scanning lidar or radar devices are used to gather wind field information upstream of wind farms or single wind turbines. Simple advection techniques proved useful to obtain information regarding the wind field reaching the downstream turbines several minutes later. For instance, a dual-Doppler radar-based forecasting methodology utilising radar data measured by two shore-based devices was successfully used to forecast wind power of individual and aggregated turbines in an offshore wind farm (VALDECABRES et al., 2018b; VALDECABRES et al., 2020). Further, several studies have investigated the use of lidar measurements for minute-scale forecasting offshore (THEUER et al., 2020a), in a near-coastal area (VALDECABRES et al., 2018b) and onshore (WÜRTH et al., 2018).

The forecast skill was hereby found to be influenced by several parameters, such as the measurement set-up and wind farm layout, the measuring range and the data availability (VALDECABRES et al., 2018a; THEUER et al., 2020a). WÜRTH et al. (2018) found that also the terrain plays a vital role in the accuracy of the forecast. Roughness as well as buoyancy effects prohibit the propagation of wind vectors across large distances, caus-

*Corresponding author: Frauke Theuer, ForWind, Institute of Physics, University of Oldenburg, Küppersweg 70, 26129 Oldenburg, Germany, e-mail: frauke.theuer@uni-oldenburg.de

ing forecasts in complex terrain not to outperform the benchmark persistence. Similarly, buoyancy forces characteristic for unstable atmospheric conditions are expected to impact the advection technique's applicability and are considered responsible for lower forecast quality (THEUER et al., 2020a). Opposed to this, THEUER et al. (2020a) found that the quality of a lidar-based power forecast of free flow turbines in an offshore wind farm showed significantly reduced prediction quality for stable cases. The authors attributed those errors mainly to the extrapolation of wind speed to hub height. Also, VALDECABRES et al. (2018b) observed forecasting errors during stable situations that were related to wind speed extrapolation.

A wind speed extrapolation to hub height is necessary for a remote sensing-based forecasting method whenever the measurements are performed at a height different from hub height. Current commercial lidar devices are in this context, contrary to radar devices, only able to measure one elevation angle when aiming to meet the requirements of short scanning periods and large scanning distances and angular ranges. Even when placing the devices on the nacelle of a turbine, dynamic turbine inclination, if recorded properly, would require a wind speed correction to hub height (BROMM et al., 2018). Despite these shortcomings, lidar-based forecasts are favourable compared to radar-based approaches, especially for offshore applications, where measurement devices need to be small and compact.

Typically, wind speed extrapolation is performed by means of a stability-corrected logarithmic wind profile (PEÑA et al., 2008). Logarithmic profiles are based on physical models, the most commonly used one being the Monin-Obukhov similarity theory (MOST). However, they are still subject to many assumptions, such as a constant wind direction with height (OPTIS et al., 2014). Additionally, uncertainty is introduced by incorrect input parameters. In a related study by the authors (THEUER et al., 2020b), uncertainty in Obukhov length L was identified as the primary contributor to extrapolation uncertainty, particularly during stable stratification. Also, wind speed uncertainties were found to have a considerable impact on the result. Similarly, SAINT-DRENAN et al. (2009) found that small errors in temperature estimation cause large errors in the extrapolated wind speed, especially during stable atmospheric conditions. KELLY and JØRGENSEN (2017) analysed the impact of roughness uncertainty on wind resource estimation. In the context of lidar-based forecasting, measuring height uncertainties are introduced by dynamic inclinations of the lidar device (ROTT et al., in review). Moreover, data processing algorithms can cause misestimations of wind speed (SCHNEEMANN et al., 2021).

Our objective in this paper is to significantly reduce errors of an existing lidar-based forecast that occur under specific atmospheric conditions due to wind speed extrapolation to hub height (THEUER et al., 2020a). Three steps contribute to this. First, we investigate how wind turbine operational data can improve the height ex-

trapolation of two new approaches. Second, we perform an analytical uncertainty estimation of the stability-corrected logarithmic profile and, for each method, Monte Carlo simulations to further account for uncertainties in lidar data processing, propagation and height extrapolation. Finally, we evaluate the different deterministic wind speed forecast methods with real measurements at free-flow turbines of an offshore wind farm. We compared the methods against the benchmark persistence and analysed different atmospheric conditions characterised by stability, wind speed increments and turbulence intensity.

2 Data description

To generate wind speed forecasts, we utilised horizontal Plan Position Indicator (PPI) lidar scans, performed at the offshore wind farm Global Tech I (GTI) in the German North Sea (Figure 1(a)) from March 2019 until June 2019. Figure 1(b) depicts the wind farm's layout with the lidar position marked in red. The wind turbines are of the type Adwen AD 5-116 with a rotor diameter of $D = 116$ m, a hub height of $z_{\text{hh}} = 92$ m and a rated power of $P_r = 5$ MW. GTI consists of 80 turbines, thus has a total capacity of $P_{\text{total}} = 400$ MW. Lidar measurements were performed by one Leosphere WindCube 200S (Serial no. WLS200S-024) placed on the transition piece (TP) of a westerly located wind turbine at a height of approximately 24.6 m above mean sea level. We used scans performed with an elevation of 0° , an averaging time of 2 s per measurement, an azimuthal resolution of 2° , spanning a total sector of 150° , and range gates ranging from 500 m to 8 000 m with 35 m spacing. The probe volume length FWHM (full width half maximum) equals approximately 70 m. The scan duration was 150 s, plus an additional measurement reset time of approximately 6 s. Four different scan orientations were distributed within the sector 112° – 300° as indicated by the coloured lines in Figure 1(b). They were selected manually depending on wind direction. The lidar scans provided information regarding the line-of-sight (LOS) velocity, carrier-to-noise-ratio (CNR), azimuth angle, range gate, and time.

To calculate atmospheric stability, air pressure, as well as humidity and air temperature data were utilised. These were measured by two sensors (Vaisala PTB330 and Vaisala HMP155) positioned close to the lidar. Moreover, the OSTIA (Operational Sea Surface Temperature and Sea Ice Analysis) data set provided sea surface temperature (SST) (GOOD et al., 2020) daily at noon, which was linearly interpolated to the lidar scans' timestamps.

For forecast evaluation, 1 Hz SCADA (supervisory control and data acquisition) data of the wind farm was available. This included wind direction, power, the operational status and a data quality flag of all turbines. Wind speed values were not measured but estimated

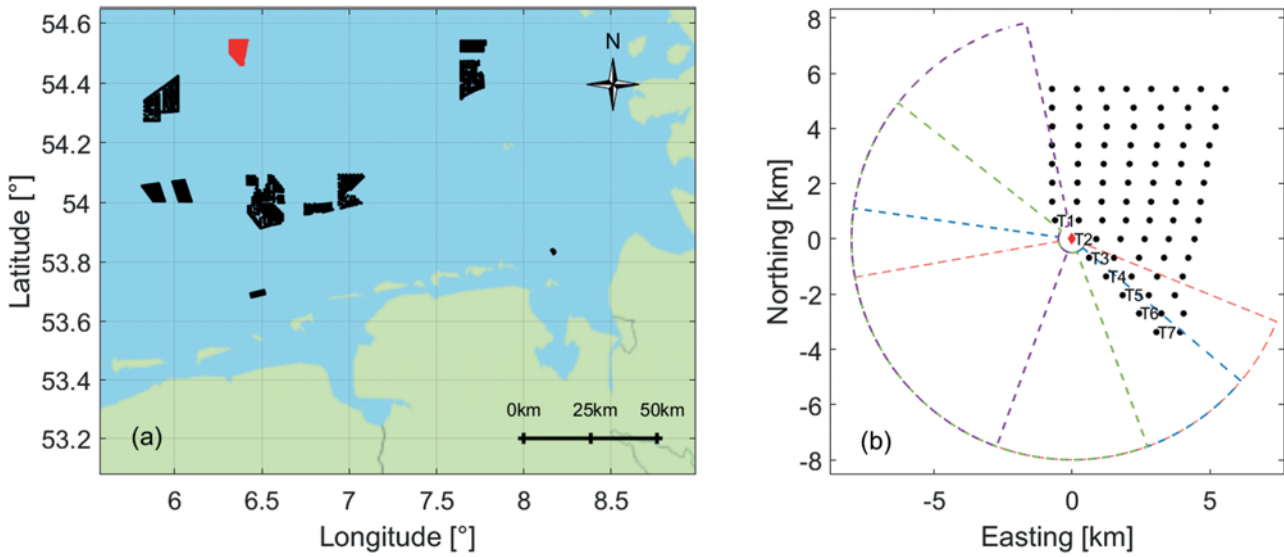


Figure 1: (a) Position of the offshore wind farm GTI in red and all other wind farms in the German and Dutch North Sea that were operational during the time of analysis from March 2019 until June 2019, in black. (b) Layout of the wind farm with the lidar's position and its four angular trajectories marked with different colours. Turbine T2 is defined as the origin of the coordinate system.

from power, pitch angle and the SCADA system's turbine power curve. Forecasts were generated and evaluated by means of 1-minute-mean wind speed values for the seven wind turbines marked as T1–T7 in Figure 1(b). We excluded lidar scans with low data availability, situations with low-quality SCADA data, wind directions $\chi < 150^\circ$ and $\chi > 310^\circ$ and turbines operating below the cut-in wind speed of 4 m s^{-1} or above the cut-off wind speed of 25 m s^{-1} at hub height. Further, only situations with simultaneously available forecasts for at least turbines T1–T4 were considered. In total, 6 493 time steps with a temporal resolution of 156 s and distributed over the measurement period with valid forecasts for at least T1–T4 were evaluated in this case study. Figure 2 summarises these cases' wind conditions, where wind speed and direction values are mean values across the lidar scans at TP height (Section 3.1).

3 Methods

In the following, the lidar-based forecasting methodology, the wind speed extrapolation of the existing forecast as well as the extrapolation approaches of the two newly developed methods are introduced. We further explain the different uncertainty estimations of wind speed extrapolation to hub height.

3.1 Lidar-based forecasting

We applied a lidar-based forecasting methodology developed by THEUER et al. (2020a) and based on the work of VALDECABRES et al. (2018a). First, lidar scans were filtered through a dynamic data filtering approach, which allows recovering data especially in far distances

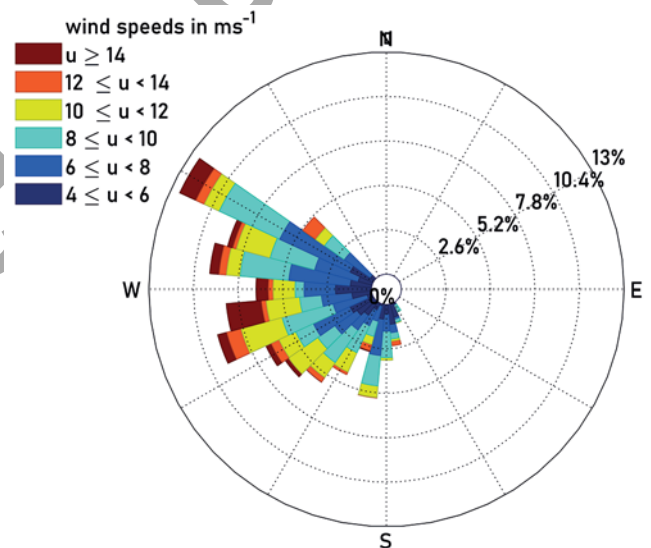


Figure 2: Distribution of wind speed and wind direction of the analysed situations. Wind speed and wind direction values are mean values across the scan area at TP height.

(BECK and KÜHN, 2017). Second, we applied a Velocity-Azimuth-Display (VAD) algorithm to determine wind direction values $\chi(r)$ individually for each range gate r . The VAD-like fit is based on the assumption of a homogeneous wind direction across azimuth angles and a negligible vertical wind speed component (WERNER, 2005). Wind direction values were further applied to determine horizontal wind speed information u_h at each measurement point using

$$u_h(r, \vartheta) = \frac{u_{\text{LOS}}(r, \vartheta)}{\cos(\vartheta - \chi(r))}, \quad (3.1)$$

where ϑ describes the azimuth angle and u_{LOS} the measured line-of-sight (LOS) velocity. In a third step, lidar scans were synchronised in time, following a methodology developed by BECK and KÜHN (2019) that was proven useful for applications in minute-scale forecasting (THEUER et al., 2020a). This step was necessary due to the device's low scanning speed, causing a time difference of 156 s between two subsequent measurements at some azimuthal position. After time synchronisation, wind vectors were propagated to the target turbines following a Lagrangian advection scheme (VALDECABRES et al., 2018a). That means the vectors were assumed to travel with their local wind speed and wind direction and to maintain their trajectory throughout the advection period. Those reaching a predefined area of influence (AoI) around the target turbine within a time interval of $k \pm 30$ s, with lead time k , were selected to contribute to the wind speed forecast. The radius of the area of influence was optimised by minimising the root-mean-squared error (rmse, Section 4.3) of a 2.5-minute-ahead wind speed forecast at turbine T2. The AoI is computed individually for each stability class and forecasting approach. Forecasts were considered valid if a number of at least 20 wind vectors reached the AoI within the considered time interval.

The translation from wind speed at measuring height to wind speed at hub height varies for the different forecasting approaches and is explained in the following subsections. Here, measuring heights z_m varied with time and range gate due to a wind turbine rotor thrust dependent tilt of the lidar device (ROTT et al., in review) and the curvature of the Earth.

In a final step, the deterministic wind speed forecast was defined as the mean magnitude of all selected wind vectors that reached the target wind turbine.

3.1.1 Temperature difference-based forecast (TDF approach)

Following THEUER et al. (2020a), wind speed vectors were extrapolated to hub height by means of the logarithmic wind profile

$$u = \frac{1}{\kappa} \sqrt{\frac{z_0 g}{\alpha_c}} \left(\ln \left(\frac{z}{z_0} \right) - \Psi \left(\frac{z}{L} \right) \right). \quad (3.2)$$

Here g denotes the gravitational acceleration, $\kappa = 0.4$ the von-Kármán constant, L describes the Obukhov length and z_0 the roughness length. The Charnock parameter was chosen as $\alpha_c = 0.011$ (SMITH, 1980). L was determined utilising a method described by SANZ RODRIGO et al. (2015) based on the measured temperature difference and is further used to estimate the stability correction term Ψ . A more detailed explanation of the wind speed extrapolation to hub height, the stability estimation and the roughness length estimation can be found in THEUER et al. (2020a). We will refer to the lidar-based forecast using this wind speed extrapolation approach as temperature difference-based forecast (TDF) from now on.

3.1.2 Wind speed profile fit-based forecast (PF approach)

As an alternative to the aforementioned temperature-difference based calculation of L and z_0 , we introduce a new approach that estimates the two parameters by fitting the logarithmic wind speed profile (Equation (3.2)) to two wind speed values at two different heights for each time step. To do so, we utilised hub height SCADA wind speed values as well as propagated wind vectors. Wind vectors were advected to the target turbine at their measuring height as part of the wind speed forecast. For the fit only vectors of past time steps, i.e. measured before the forecast's initialisation, were considered. We used average wind speeds and average heights of wind vectors originating from the 30-minute-period before forecast initialisation, with their magnitude weighted according to their age. Thus, we assume the derived wind speed profiles will persist until the time of the forecast. As weighting function a Gaussian distribution centered around the time of the forecast initialisation and with a standard deviation of 15 minutes was used. Also hub height wind speeds were weighted and averaged. The fit used the previously calculated values of L and z_0 (Section 3.1.1) as an initial guess. However, this methodology is in principle independent of meteorological measurements at the site. Wind speed profile fits were performed individually for each of the analysed turbines. We will refer to this newly introduced approach as profile fit-based forecast (PF) in the following.

3.1.3 Tendency-based forecast (TF approach)

To reduce the extrapolation distance δz , i.e. the difference between measuring height and the height of interest, we introduce the tendency-based forecasting approach (TF). Here, consecutive wind speed forecasts at time instants t_{i-1} and t_i and corresponding measuring heights $z_m(t_{i-1})$ and $z_m(t_i)$ are determined using the methodology described at the beginning of Section 3.1. Hereby, t_{i-1} describes the current time and t_i the time to be forecasted. The wind speed at hub height dependent on time $u_{\text{hh}}(t)$ can be expressed by means of the wind speed at measurement height $u_m(t)$ and a time dependent correction factor $c_{\text{ex}}(t)$:

$$u_{\text{hh}}(t) = \frac{\ln \left(\frac{z_{\text{hh}}}{z_0(t)} \right) - \Psi \left(\frac{z_{\text{hh}}}{L(t)} \right)}{\ln \left(\frac{z_m(t)}{z_0(t)} \right) - \Psi \left(\frac{z_m(t)}{L(t)} \right)} u_m(t) = c_{\text{ex}}(t) u_m(t). \quad (3.3)$$

Equation (3.3) can further be used to express $u_{\text{hh}}(t)$ at the two consecutive time steps t_i and t_{i-1} . The quotient of the wind speed at hub height and the extrapolation from the measurement height is equated for the two time steps. Rearranging this identity yields

$$u_{\text{hh}}(t_i) = \frac{c_{\text{ex}}(t_i)}{c_{\text{ex}}(t_{i-1})} \frac{u_m(t_i)}{u_m(t_{i-1})} u_{\text{hh}}(t_{i-1}). \quad (3.4)$$

Obukhov length L and roughness length z_0 can be determined using meteorological measurements, following

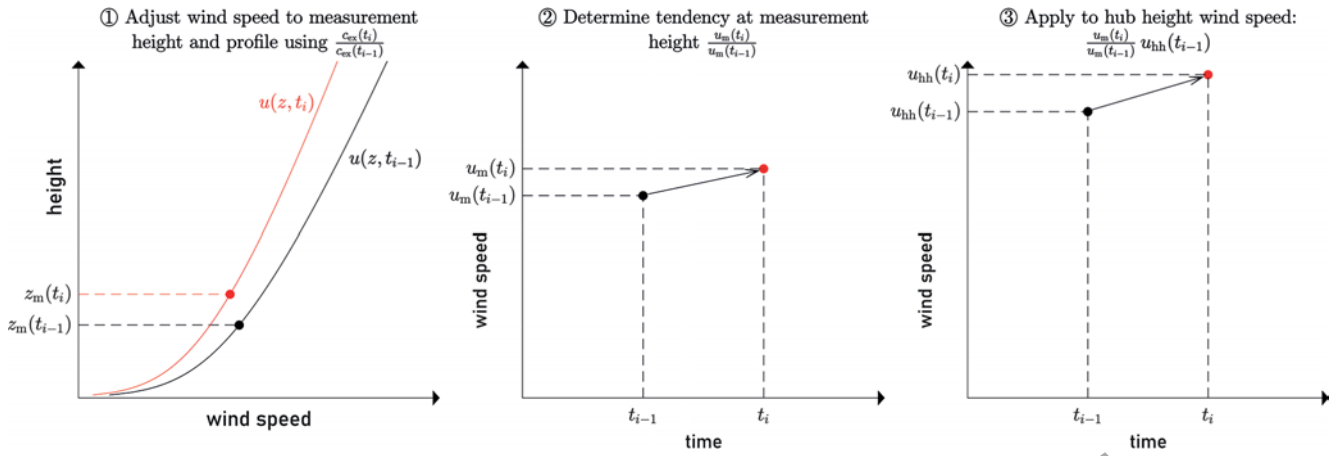


Figure 3: Tendency-based forecasting approach. First, the wind speed at time step t_{i-1} is adjusted to the profile described by L and z_0 and the measuring height z_m at t_i . Then a wind speed tendency at measuring height is determined and in a third step applied to wind speed observations at hub height.

the approach described in Section 3.1.1, or by means of the fit described in Section 3.1.2. When assuming the atmospheric conditions do not vary significantly from t_{i-1} to t_i , i.e. $L(t_i) \approx L(t_{i-1})$ and $z_0(t_i) \approx z_0(t_{i-1})$ the expression (3.4) simplifies to

$$u_{hh}(t_i) = \frac{\ln\left(\frac{z_m(t_{i-1})}{z_0(t_i)}\right) - \Psi\left(\frac{z_m(t_{i-1})}{L(t_i)}\right)}{\ln\left(\frac{z_m(t_i)}{z_0(t_i)}\right) - \Psi\left(\frac{z_m(t_i)}{L(t_i)}\right)} \frac{u_m(t_i)}{u_m(t_{i-1})} u_{hh}(t_{i-1}). \quad (3.5)$$

Figure 3 illustrates the methodological steps of the TF: The term $\frac{c_{ex}(t_i)}{c_{ex}(t_{i-1})}$ in Equation (3.4) can be understood as the adjustment of the measured wind speed at t_{i-1} to atmospheric conditions and measuring height at t_i . When assuming constant L and z_0 , the expression equals the correction factor of a wind speed extrapolation from $z_m(t_i)$ to $z_m(t_{i-1})$ (left fraction of Equation (3.5)). The difference between $z_m(t_i)$ and $z_m(t_{i-1})$ is hereby significantly smaller than that of $z_m(t_i)$ and z_{hh} . We thus avoid the extrapolation across large height differences. Subsequently, the two consecutive forecasts at t_{i-1} and t_i at measurement height are used to derive a wind speed tendency, i.e. the relative change of wind speed from one time step to the other, expressed by the term $\frac{u_m(t_i)}{u_m(t_{i-1})}$ in Equation (3.4). The forecasted tendency is then applied to the current hub height wind speed $u_{hh}(t_{i-1})$, i.e. SCADA wind speed, to determine the future one $u_{hh}(t_i)$. Similarly as for persistence, the wind speed forecast in this method is based on the current wind speed observation. The lidar-based approach, however, allows to include information of the approaching wind field additionally.

In course of this work we tested three variants of the TF, i) using Equation (3.3) and meteorological parameters, ii) using Equation (3.3) and fitted parameters and iii) using Equation (3.5) and meteorological parameters. No significant quality differences were observed between the three variants. In the following we will therefore show the results of the simplified case iii) only.

3.2 Uncertainty estimation of lidar-based forecasting approaches

Previous studies have suggested that lidar-based forecasting errors are largely caused by errors in wind speed extrapolation (THEUER ET AL., 2020a). We therefore performed an analytical uncertainty estimation of the wind speed extrapolation based on a logarithmic stability-corrected wind profile. This analytical approach does not account for uncertainties related to the wind vector propagation, but focuses solely on the wind speed extrapolation. It is considered a good representation of the uncertainty for the TDF only, as the wind profile of the PF is based on a fitting approach and the TF only indirectly applies the logarithmic profile. Nevertheless, this uncertainty estimation is considered valuable to characterise the shortcomings of wind speed extrapolation by means of a logarithmic profile in more detail.

As a second method for uncertainty estimation, we performed Monte Carlo simulations. They allow to determine uncertainties related to all three approaches and include uncertainties related to the lidar data processing, wind vector propagation and height extrapolation. Moreover, they consider possible numerically introduced uncertainties and provide a metric that is directly linked to the case study analysed in this work.

3.2.1 Uncertainty estimation related to the logarithmic wind profile

A theoretical uncertainty estimation is possible based on the analytical expression for the stability-corrected logarithmic wind profile (Equation (3.2)). We applied Gaussian uncertainty propagation to Equation (3.3) to determine the total uncertainty Δ_y

$$\Delta_y = \sqrt{\sum_i \left(\left| \frac{\partial y}{\partial x_i} \right| \Delta x_i \right)^2}, \quad (3.6)$$

using the uncertainties of the input variables Δx_i .

Table 1: Input variables used for the analytical uncertainty estimation and standard deviations of error distributions used for the Monte Carlo simulations. For the analytical uncertainty estimation, we used twice the stated standard deviation.

variable	input value	standard deviation
LOS wind speed	-	0.2 m s^{-1}
azimuth	-	0.025°
wind direction	-	1°
propagated wind vectors	-	0.1 m s^{-1}
pitch	-	0.025°
roll	-	0.025°
measurement height	24.6 m	0.3 m
SCADA wind speed	-	0.05 m s^{-1}
wind speed at lidar position	8.2 m s^{-1}	0.05 m s^{-1}
air temperature	{1, 1.2, ..., 23} °C	0.05 °C
water temperature	{6, 6.2, ..., 18} °C	0.1 °C
pressure	1011.81 hPa	0.15 hPa
humidity	80.69 %	0.6 %
roughness length	$9 \cdot 10^{-5} \text{ m}$	$4.5 \cdot 10^{-6} \text{ m}$

The wind speed extrapolation uncertainty Δu_{hh} as a function of the measured wind speed uncertainty Δu_m , the roughness length uncertainty Δz_0 , the measurement height uncertainty Δz_m and the stability term uncertainty $\Delta\Psi$ was derived in more detail by THEUER et al. (2020b). The uncertainty of the stability correction term $\Delta\Psi$ was expressed as a function of the Obukhov length uncertainty ΔL and the height uncertainty Δz . While so far ΔL was assumed to be a constant, we here estimated it using uncertainties in meteorological measurements used to calculate L . Input variables were the TP height z_{TP} and wind speed at TP height u_{TP} , air and water temperature T_{TP} and T_0 , humidity H and pressure p , and all associated uncertainties. More details on the estimation of L and its uncertainty can be found in SCHNEEMANN et al. (2021). Table 1 summarises the values of all input variables used for the analytical uncertainty estimation. Air and water temperature, pressure, humidity and wind speed were defined in accordance with the measured values during the analysed time period. Uncertainties were chosen following typical values suggested in the respective sensor's user manual. All uncertainty terms used in the analytical uncertainty estimation correspond to twice the standard deviation indicated in Table 1 and are thus considered to include 95 % of all errors.

3.2.2 Uncertainty estimation related to lidar data processing, propagation and height extrapolation

For uncertainty estimation of lidar data processing, wind vector propagation and the PF's and TF's height extrapolation no analytical description is available. Thus, no analytical uncertainty estimation can be computed. However, Monte Carlo simulations for each of the three approaches can be applied. Monte Carlo simulations re-run the forecast N times with varying input variables. The Monte Carlo runs provide many possible outcomes

based on the variations of the input parameters. The standard deviation of these is considered a representation of the results' uncertainty. The input parameters were randomly selected using previously defined error distributions (ZHAO et al., 2018). In this case, we performed simulations with $N = 1\,000$ repetitions and errors normally distributed around a mean error value of zero. The wind fields determined from lidar scans were hereby subject to LOS wind speed, azimuth and wind direction errors. Errors in wind vector propagation were expressed by adding a random wind speed error to vectors contributing to the forecast. Height errors were characterised in terms of pitch and roll error, which define the lidar's tilt (ROTT et al., in review). Thus, height errors increased with measurement distance to the device. A visualization of pitch and roll uncertainty and other uncertainties related to long-range lidar measurements can be found in Figure 2 of SCHNEEMANN et al. (2021). Errors in L and z_0 were realised considering errors in air and water temperature, pressure, humidity and the wind speed at lidar position.

For each analysed time step, a new set of N random errors was selected from each variable's error distribution. We are aware that errors are not uncorrelated between time steps, however, we chose this approach for simplicity reasons. The only errors we consider correlated between time steps are LOS wind speed and azimuth pointing errors, and thus here the same N errors were assigned to all analysed time steps. Also this assumption can be understood as a simplification.

The uncertainties assigned to the input variables are summarised in Table 1.

4 Results

In the following, we present the results of the two uncertainty analyses (Section 4.1). Further, the case study is analysed, evaluating the estimated vertical wind speed profiles (Section 4.2) and the minute-scale wind speed forecasts (Section 4.3).

4.1 Uncertainty estimation of lidar-based forecasting approaches

4.1.1 Uncertainty estimation related to the logarithmic wind profile

As described in Section 3.2.1, we analysed the dependency of ΔL and further Δu_{hh} on L . We calculated ΔL , with input variables defined in Table 1. Figure 4(a) shows the dependency of ΔL on L on the left y-axis. ΔL approaches zero for $L \rightarrow 0 \text{ m}$ and infinity for $L \rightarrow \infty$. At $L = 200 \text{ m}$, ΔL has already increased to 49 m. For $L = -200 \text{ m}$ the uncertainty is slightly smaller with $\Delta L = 46 \text{ m}$, due to the definition of L . The curve's overlapping regions were caused by varying absolute temperature values, which resulted in the same value for L , but slightly differing ΔL .

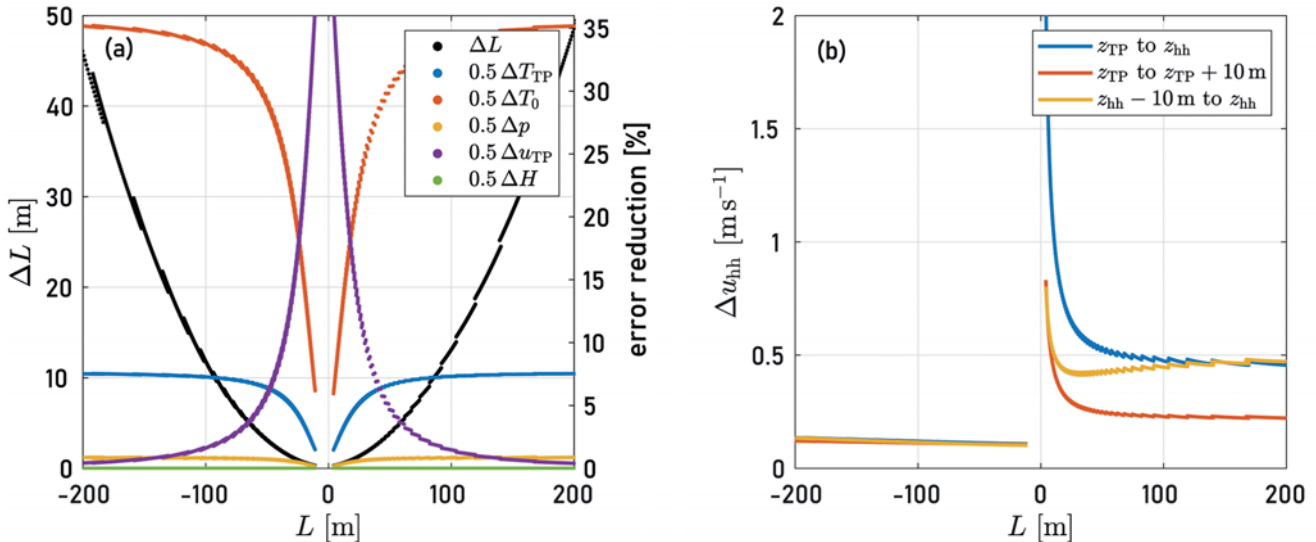


Figure 4: Analytical estimation of the wind speed extrapolation uncertainty. In (a) the uncertainty of L is shown in black with ΔL on the left y-axis. As coloured lines on the right y-axis, the reduction of ΔL for reducing the error of one of the contributors by 50 % is visualised. In (b) the wind speed extrapolation uncertainty Δu_{hh} is depicted for varying extrapolation distances dependent on L .

To understand the impact of the different contributions to the overall uncertainty, we reduced the individual uncertainty contributions to 50 % of their initially defined value. The reduction of ΔL is shown on the right y-axis for variations of ΔT_{TP} , ΔT_0 , Δp , Δu_{TP} and ΔH . While an increase of accuracy for humidity and pressure had none to little impact, a reduction of Δu_{TP} could significantly reduce ΔL , especially during very stable and very unstable situations ($|L| \rightarrow 0$). Approaching neutral situations, the most considerable impact can be attributed to the temperature uncertainties, particularly the water temperature uncertainty. As in very stable or unstable scenarios, the temperature errors are small compared to the temperature difference; they have a smaller impact on the stability estimation.

Figure 4(b) visualises how the wind speed extrapolation uncertainty Δu_{hh} changes with L . Variables were defined as stated in Table 1. THEUER et al. (2020b) have previously found that the two main contributors to the wind speed extrapolation uncertainty are the components of the stability correction terms, i.e. $\left| \frac{\delta u_{hh}}{\delta \Psi} \right| \Delta \Psi$, and the wind speed component, i.e. $\left| \frac{\delta u_{hh}}{\delta u_m} \right| \Delta u_m$. We thus focus on these contributors here. In neutral conditions, i.e. $|L| \rightarrow \infty$, the wind speed component contributes strongly to Δu_{hh} . The stability correction terms Ψ_m and Ψ_{hh} become zero while $\Delta \Psi_m$ and $\Delta \Psi_{hh}$ approach a limit related to water and air temperature uncertainties and the considered heights. When L approaches zero in stable cases, both $\Delta \Psi$ as well as $|\Psi|$ approach infinity. The overall contributions of the stability terms approach infinity and they dominate Δu_{hh} . In unstable cases this is also true; however, $\Delta \Psi$ will increase only from very small $|L|$ onwards, dependant on the input parameters. Therefore this increase is hardly visible in Figure 4(b) and will most likely not impact many of the considered cases.

Further investigation has shown that Δu_{hh} and all of its sub-components increase with extrapolation distance, as visualised in Figure 4(b). Here, the wind speed extrapolation uncertainty Δu_{hh} is shown for reduced extrapolation distances of 10 m in a lower region of the wind speed profile in red and in a higher one in yellow. As a change of extrapolation distance was found to mainly impact errors associated with the stability terms and wind speed, its reduction will have the most considerable effect during stable stratification when these terms have a larger contribution to the wind speed extrapolation uncertainty (THEUER et al., 2020b). It is also visible that uncertainties are smaller in lower regions of the logarithmic wind profile.

4.1.2 Uncertainty estimation related to lidar data processing, propagation and height extrapolation

Figure 5 depicts the standard deviation of the Monte Carlo simulations σ_{mc} described in Section 3.2.2 dependent on Obukhov length L with 117 values per bin and 95 % confidence intervals visualised as error bars. In accordance with the results of the analytical error analysis of the wind speed extrapolation (Section 4.1.1) values are larger in stable compared to unstable situations for the TDF, with particularly large uncertainties during very stable situations. The TF shows a similar pattern during stable cases, however, with significantly lower uncertainties. For both approaches the large uncertainty in u_{hh} , i.e. σ_{mc} , is caused by the high sensitivity of c_{ex} to the input variables. As for the TF the ratio of c_{ex} values of two consecutive time steps is considered, its variation does have a smaller impact on the overall result than for the TDF. Similarly, also variations of wind speed have

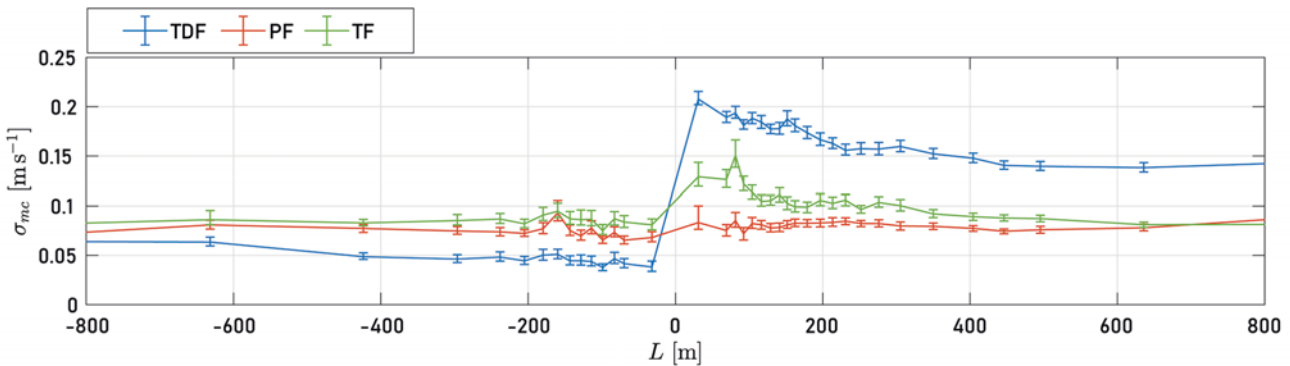


Figure 5: Standard deviation of Monte Carlo simulations dependent on Obukhov length L for the different forecasting methodologies. The 95 % confidence intervals are visualised as error bars. Each bin contains 117 values.

less influence on the TF. During unstable cases, the uncertainty of SCADA wind speed dominates the overall uncertainty of the TF, resulting in larger uncertainties compared to the TDF.

The profile fit shows almost constant σ_{mc} for different L . The fitting algorithm can adjust for variations in the input variables. Likewise to the TF, the uncertainty of SCADA wind speeds dominates σ_{mc} . The PF's uncertainty is larger than the TDF's during unstable cases but can outperform both TDF and TF during stable situations.

Overall, the results indicate that the two alternative approaches of wind speed extrapolation, i.e. PF and TF, are less sensitive to flawed estimations of input parameters during stable situations, which means a lower uncertainty can be assigned to the forecasts. One should, however, be aware that the absolute values σ_{mc} are strongly dependent on the error distributions' standard deviations. Further, the impact of different variables on the results varies for different approaches.

4.2 Estimation of vertical wind speed profiles

In Sections 3.1.1 and 3.1.2 we used two methods to determine the parameters z_0 and L . The first is based on a physical estimation (TDF), while the latter is based on an empirical fit (PF). This section compares the estimated parameters of TDF and PF to gain insight into the advantages and shortcomings of the different methodologies.

Figure 6(b) plots the corresponding values of the roughness length z_0 against each other, using the two methods for turbines T1–T4. Here, two clusters can be distinguished. In the first, the TDF and PF roughness lengths are scattered around the black diagonal line, indicating perfect agreement. In the second cluster, the PF values are about 4.5 times larger than the ones of the TDF, which is discussed in Section 5.1. Figure 6(a) visualises the distribution of L for both the TDF and PF with bins of 50 m width. In the histogram, it stands out that the number of very unstable cases, i.e. cases with $-50 \text{ m} < L < 0 \text{ m}$ is much larger for the fit (PF) than the temperature-difference estimation (TDF). This can be explained with the help

of Figure 7(a), which shows the relation of L and the wind speed difference between measuring height and hub height $\delta u = u_{hh} - u_m$ for both the TDF and PF. As reference the wind speed difference determined using the MOST is shown in black dependent on L and for mean values of measuring height $z_m = 36 \text{ m}$ and roughness length $z_0 = 9 \cdot 10^{-5} \text{ m}$. Additionally, the frequency of stability classifications is given within each panel in Figure 8(a) as a percentage of the total number of values considered. We defined the five stability classes very unstable ($-200 \text{ m} \leq L < 0 \text{ m}$), unstable ($-1000 \text{ m} < L < -200 \text{ m}$), neutral ($|L| \geq 1000 \text{ m}$), stable ($200 \text{ m} < L < 1000 \text{ m}$) and very stable ($0 \text{ m} < L \leq 200 \text{ m}$), which are shown on the x-axis for the TDF and on the y-axis for the PF. Panels positioned on the diagonal therefore represent situations with the same stability class for both the TDF and PF. Figure 8 will be presented in more detail in Section 4.3.1. The fitting algorithm classified profiles as very unstable when wind speed values decreased or stayed constant with height. While for situations $\delta u > 0 \text{ m s}^{-1}$, the resemblance of the PF results and the theoretical estimation by means of MOST is high, for very unstable cases, δu determined with the MOST approaches 0 m s^{-1} . Those cases also corresponded to the situations with increased values of z_0 as visualised in Figure 7(b). During many situations z_0 stayed almost constant at a low value, i.e. L was the main parameter used to influence the profile. When L was quite restricted by the negative wind speed difference with height, z_0 played a more important role, thus was assigned a larger value. While most of these situations were estimated as unstable (Figure 7(a)) by means of the temperature difference, 19 % were defined as neutral and 15 % as stable. An evaluation (cf. Figure 8(a)) revealed that about 3.5 % of all analysed cases were classified as stable by the TDF but fitted as unstable cases by the PF. That includes, besides situations with decreasing wind speed with height, also many with only slightly increasing wind speed of up to approximately 0.6 m s^{-1} . Conversely, in 4.5 % of all situations, cases classified as unstable by the TDF were classified as stable by the PF. Here, the increase of wind speed with height was larger with about 0.8 m s^{-1} to 2.0 m s^{-1} .

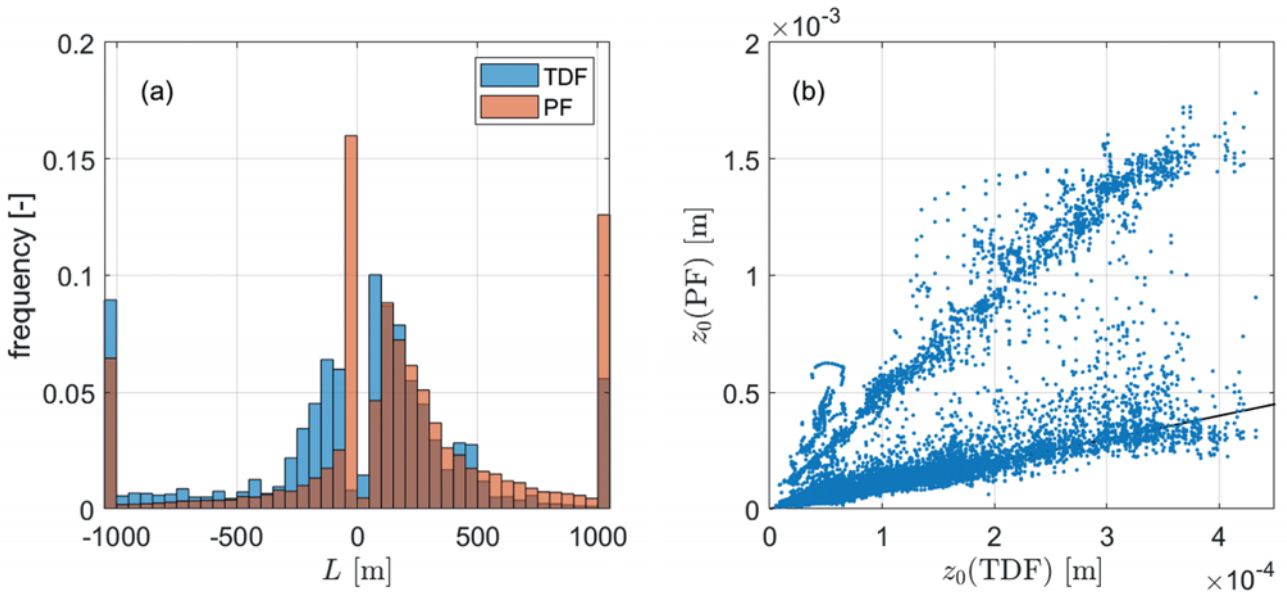


Figure 6: Comparison of TDF and PF wind profile parameters. In (a) the histograms of the Obukhov length L are shown in bins with 50 m width. The outermost bins represent all values with $L < -1000$ m and $L > 1000$ m, respectively. In (b) the roughness length z_0 is compared for the TDF on the x-axis and the PF on the y-axis. The black line indicates perfect agreement between z_0 of TDF and PF.

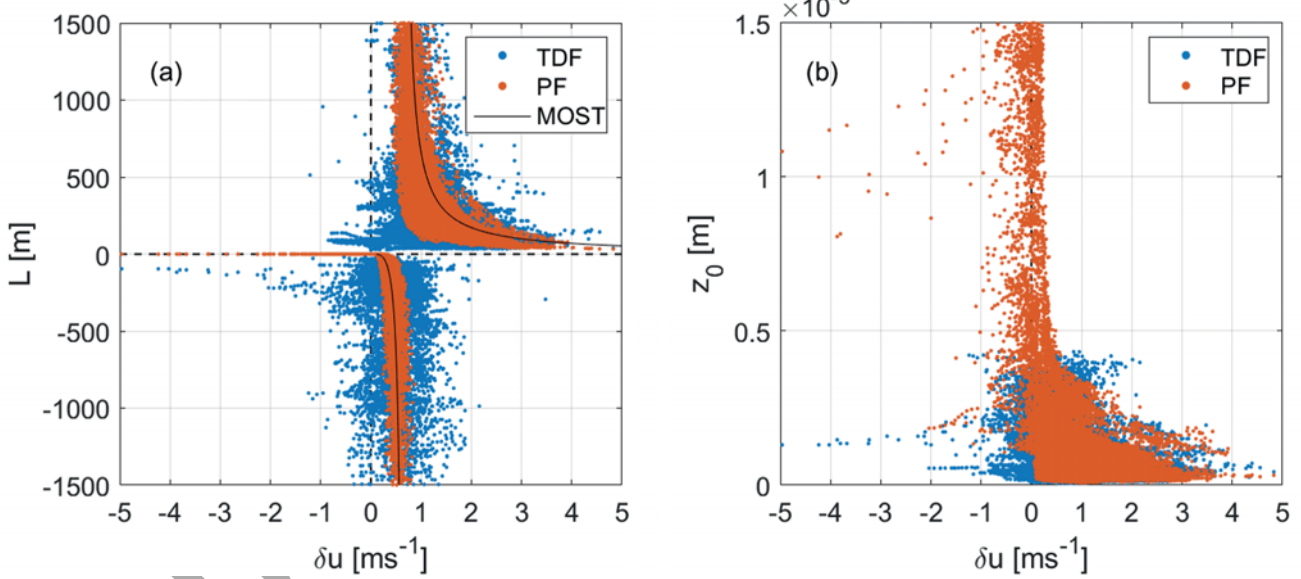


Figure 7: Relation between the predicted wind speed difference from measuring to hub height δu and (a) Obukhov length L and (b) roughness length z_0 of TDF and PF. The black line in (a) depicts the wind speed difference determined using the MOST depending on L for representative values of measuring height and roughness length.

4.3 Minute-scale wind speed forecasting

5-minute-ahead wind speed forecasts at the turbines T1–T7 were generated using the three introduced extrapolation approaches, i.e. i) the temperature difference-based forecast (TDF approach), ii) the wind speed profile fit-based forecast (PF approach) and iii) the tendency-based forecast (TF approach). As a reference a persistence forecast was used. Persistence is considered a benchmark in minute-scale forecasting and is based on the assumption that the current value will persist un-

til the time of the forecast (WÜRTH et al., 2019). For further analysis only situations with valid forecasts for all three approaches and simultaneously available forecasts for turbines T1–T4 were considered (Section 2). The root-mean-squared error (rmse)

$$\text{rmse} = \sqrt{\frac{1}{N} \sum_{i=1}^N (\text{fc}_i - \text{obs}_i)^2} \quad (4.1)$$

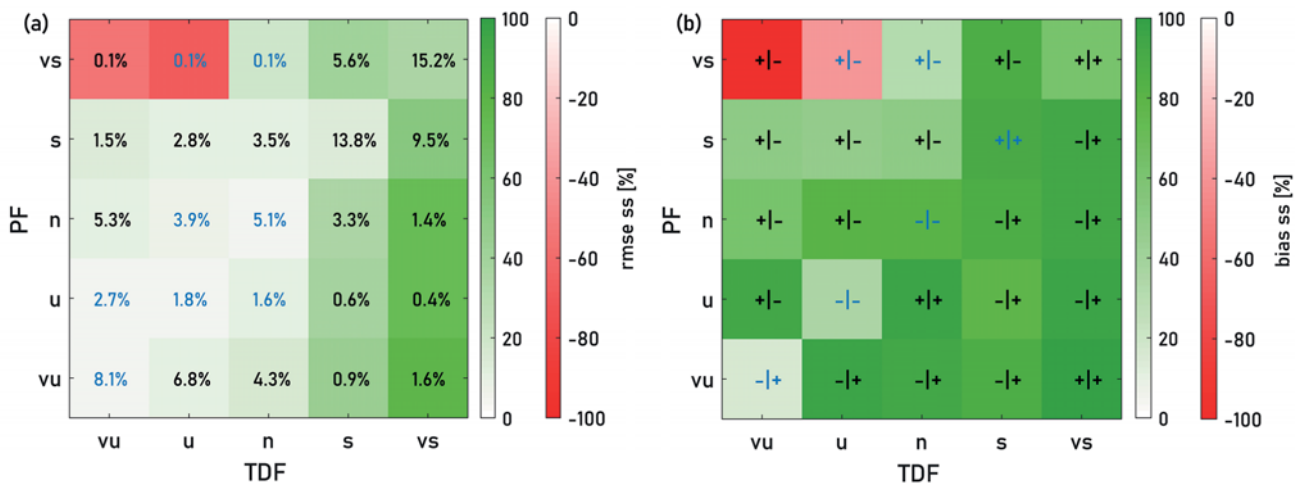


Figure 8: Comparison of 5-minute-ahead wind speed forecast skill of the TDF and the PF. In (a) TDF stability classes are shown on the x-axis, while PF ones are plotted on the y-axis. The values within the panels indicate the percentage of respective stability classifications with respect to all cases analysed. The colour-scale visualises the PF's skill score compared to the TDF in percent. Subfigure (b) shows the bias skill score, respectively. Here, the sign of the bias is indicated within the panel (PF|TDF). Blue values and signs indicate statistically insignificant results.

and the bias

$$\text{bias} = \frac{1}{N} \sum_{i=1}^N (\text{fc}_i - \text{obs}_i) \quad (4.2)$$

of the forecasts fc_i were determined by comparison with the observations obs_i , i.e. 1-minute-mean SCADA wind speed values. Here, N denotes the number of forecasts considered in the (sub-)dataset.

To compare the forecast skill to a reference forecast, the skill score expressed as percentage

$$\text{rmse ss} = 100 \left(1 - \frac{\text{rmse}}{\text{rmse}_{\text{ref}}} \right) \quad (4.3)$$

was used. The bias skill score (bias ss) was determined accordingly. The skill score equals 100 % for a perfect forecast with $\text{rmse} = 0$ or $\text{rmse} \ll \text{rmse}_{\text{ref}}$ and is negative for $\text{rmse} > \text{rmse}_{\text{ref}}$.

In the following, we first assess the profile fit and tendency approach applied to T1–T4 before comparing the skill of all forecasting methodologies.

4.3.1 Comparison of wind speed profile fit-based forecast and temperature difference-based forecast

The previous section revealed the partially large differences between the stability classes defined by the TDF and the PF. We therefore analyse how the estimated stability class impacts the forecast accuracy of the two methods in more detail. Figure 8 compares the forecast skill of the temperature difference-based forecast and the profile fit respectively. In both sub-figures it matches the stability classes derived by the TDF on the x-axis with the stability classes estimated for the PF on the

y-axis. The panels positioned on the diagonal hence depict the identical stability class estimated by both approaches. The values within the panels in Figure 8(a) indicate the frequency of occurrence of each classification with respect to all cases analysed. Figure 8(a) visualises the profile fit's rmse skill score with the TDF rmse as the reference on a colour scale. The skill score of the bias' magnitude is shown in Figure 8(b), with the bias' sign of each of the two methods indicated within each panel (PF|TDF). In both sub-plots panels marked by blue writing indicate that the results are not statistically significant. Significance was determined by comparing 95 % confidence intervals of both data samples, as suggested by CUMMING (2009). For most of the shown panels, indicated in green, the PF's rmse was reduced as compared to the TDF. The largest rmse skill score of 77 % was observed for situations defined as very stable by the TDF and as very unstable by the PF, visualized by the deep green panel in the lower right corner. In many of these situations, classified as very stable by the TDF, wind speeds were found to decrease or stay constant with height, and were thus categorised as very unstable profiles by the PF's fitting algorithm. Consequently, the substantial overestimation of wind speed and large rmse caused by the extrapolation using a very stable profile were reduced. Strongly positive skill scores were generally observed for situations classified as stable or very stable by the TDF and those classified as very unstable by the PF due to the same reasons. As indicated by Figure 8(b) also the bias was in those situations improved by at least 62 %. In total, such cases were observed in 72 % of all analysed situations.

Several cases with comparably small skill scores, i.e. TDF and PF have almost the same result, indicated by light coloured panels near the main diagonal, can be observed. A number of these were determined not to be

statistically significant. That means, for instance, due to a low number of forecasts within that category or only small differences between the scores of TDF and PF, it is ambiguous whether the profile fit leads to a reduction of forecasting errors. A reduction of the rmse and bias forecast skill was observed for situations classified as very unstable or unstable by the TDF and as very stable by the PF, visualized by the red panels in the upper left corner. They show a rmse skill score of -53% and -68% , respectively and a bias skill score of -156% and -39% , respectively. Both panels contain only a very small number of values and the scores of the latter can be considered insignificant.

4.3.2 Influence of height extrapolation on tendency-based forecast

The uncertainty analysis with the Monte Carlo-simulations revealed the sensitivity of the TF to errors in the SCADA wind speeds and possible wind vector propagation and lidar data processing, while the approach was more robust with respect to wind speed extrapolation uncertainties. In order to further improve the TF approach we assessed its quality dependent on extrapolation distance δz . Extrapolation distance is in this context defined as the difference of measuring height between the two consecutive wind speed forecasts used to determine the wind speed tendency, i.e. $\delta z = z_m(t_i) - z_m(t_{i-1})$. In Figure 9 rmse and bias dependent on δz are visualised, summarising the results of turbines T1–T4 and distinguishing between atmospheric stability. In stable cases, each bin contains 503 values, in unstable cases 574 values.

The extrapolation distance δz is a consequence of the varying propagation distance of the contributing wind vectors to the lidar and the device's varying tilt. As expected, in Figure 9(a) forecast skill decreases for larger $|\delta z|$. As both the varying tilt and the varying distance of wind vectors to the lidar are related to wind speed changes, more larger extrapolation distances were observed during unstable cases. While in stable situations 90 % of all analysed values lay below $|\delta z| < 1\text{ m}$, in unstable situations it was only 67 %. The tendency forecasts overestimated wind speed for positive δz and underestimated it during negative ones (Figure 9(b)).

4.3.3 Comparison of the three forecasting methods

Figure 10 compares rmse and bias for the two new forecasting approaches, the previously introduced lidar-based forecast and persistence distinguishing between unstable (a, d), neutral (b, e) and stable (c, f) situations individually for the seven analysed turbines. Hereby, stable cases are defined as $0\text{ m} < L \leq 1000\text{ m}$, unstable cases as $-1000\text{ m} \leq L < 0\text{ m}$ and neutral ones as $|L| > 1000\text{ m}$. We only considered situations with simultaneously available forecasts for all turbines and approaches. Generally, forecasts are most accurate in stable situations, followed by neutral and unstable ones. Only exception are the distinct errors of the TDF ob-

served during stable situations. Here, the bias indicates a strong overestimation of wind speed for all analysed turbines, except T5. Most accurate during stable situations is persistence, closely followed by the TF. PF, TF and persistence all show a bias close to zero. For unstable cases, the PF yields the lowest rmse, outperforming persistence for turbines T1–T6. The TDF and, in particular, the TF show a slightly larger rmse; however, they are also outperforming persistence for most cases. A positive bias, especially large for T6 and T7, can be observed for both the TDF and PF. Also in neutral situations, the PF can outperform all other approaches. The bias is close to zero for all four forecasts; only the TDF shows a distinct overestimation for T1, T2, T6 and T7.

In the following, we analyse the forecast skill dependent on atmospheric conditions in more detail. To do so, we summarise the results of turbines T1–T4. We excluded turbines T5–T7 from this analysis due to their low forecast skill and availability. In all of the following figures (i.e. Figure 11–13), 95 % confidence intervals are visualised as error bars. Figure 11 depicts the dependency of rmse and bias on the Obukhov length L for all forecast methodologies. Each bin contains 716 values. Similar to Figure 10, all approaches are able to outperform persistence during unstable situations; however, not during stable ones. PF and TF beat the TDF during stable situations in terms of rmse, during unstable cases the TF can not outperform the TDF. The rmse values are generally lower for stable as compared to unstable cases except for the TDF. A large peak is visible for very stable cases with $0\text{ m} < L < 100\text{ m}$ with a rmse of up to 1.6 m s^{-1} and a bias of 1.3 m s^{-1} . Approaching neutral situations, the TDF's bias shows a slight underestimation of wind speed. The bias of PF, TF and persistence fluctuates around zero for the entire range of L .

In Figure 12 the rmse dependent on the 5-minute wind speed increment from the forecast's initialisation time to the forecasted time for both stable and unstable cases is visualised. Each bin contains 503 values for stable and 574 values for unstable situations. Due to the definition of persistence, its rmse and bias are of the same magnitude as the increment itself. For the TDF the forecast skill is significantly lower for stable than for unstable cases as confirmed by previous results. Both the PF and the TF show lower rmse during stable stratification. For all three approaches, the rmse only slightly increases with increasing increment. The PF is hereby least sensitive to the magnitude of the wind speed increment. Consequently, the lidar-based forecasting methodologies are able to outperform persistence during changes in wind speed exceeding 0.5 m s^{-1} to 0.6 m s^{-1} . During unstable stratification large wind speed increments can be most accurately forecasted by the PF, followed by the TDF and the TF. While during unstable stratification about 34 % to 41 % of all values show increments larger than the determined threshold of 0.5 m s^{-1} to 0.6 m s^{-1} , this is the case only for 10 % to 16 % during stable stratification.

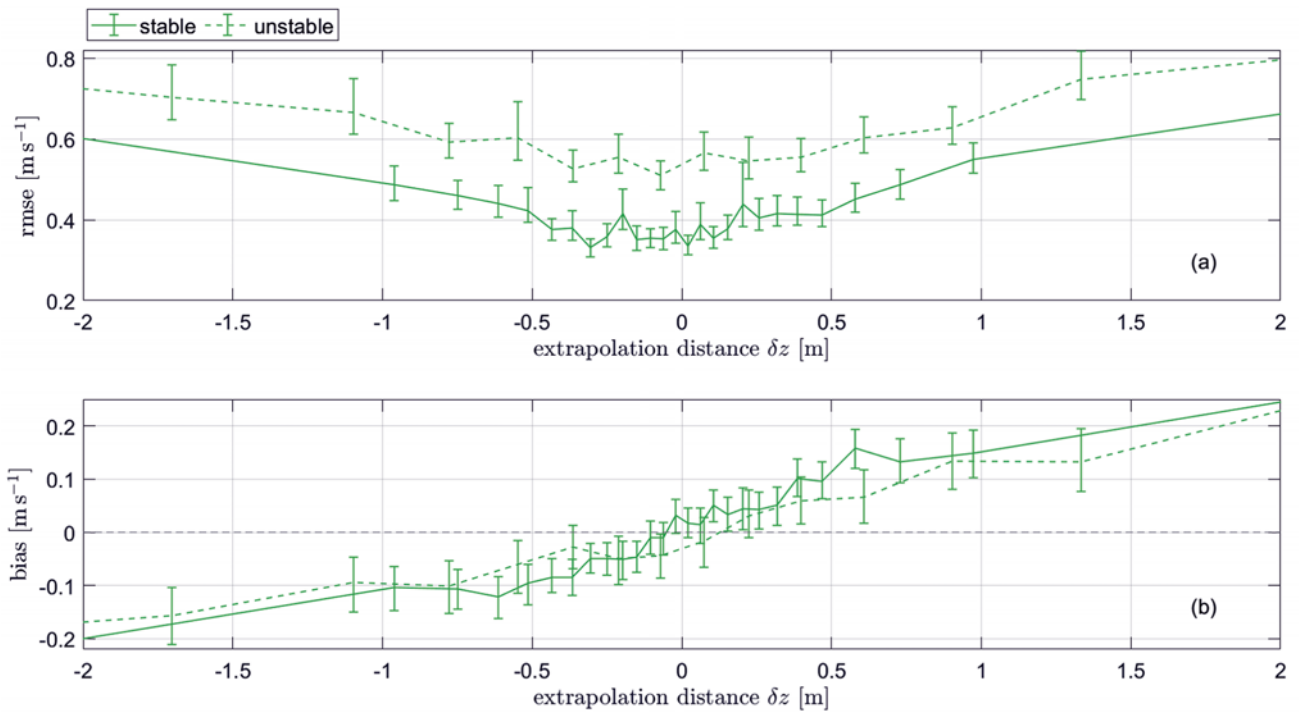


Figure 9: Forecast quality of the 5-minute ahead wind speed forecast dependent on extrapolation distance δz . The TF's (a) rmse and (b) bias, distinguishing between stable and unstable situations, are depicted. The 95 % confidence intervals are visualised as error bars. For stable cases each bin contains 503 values, for unstable cases 574 values.

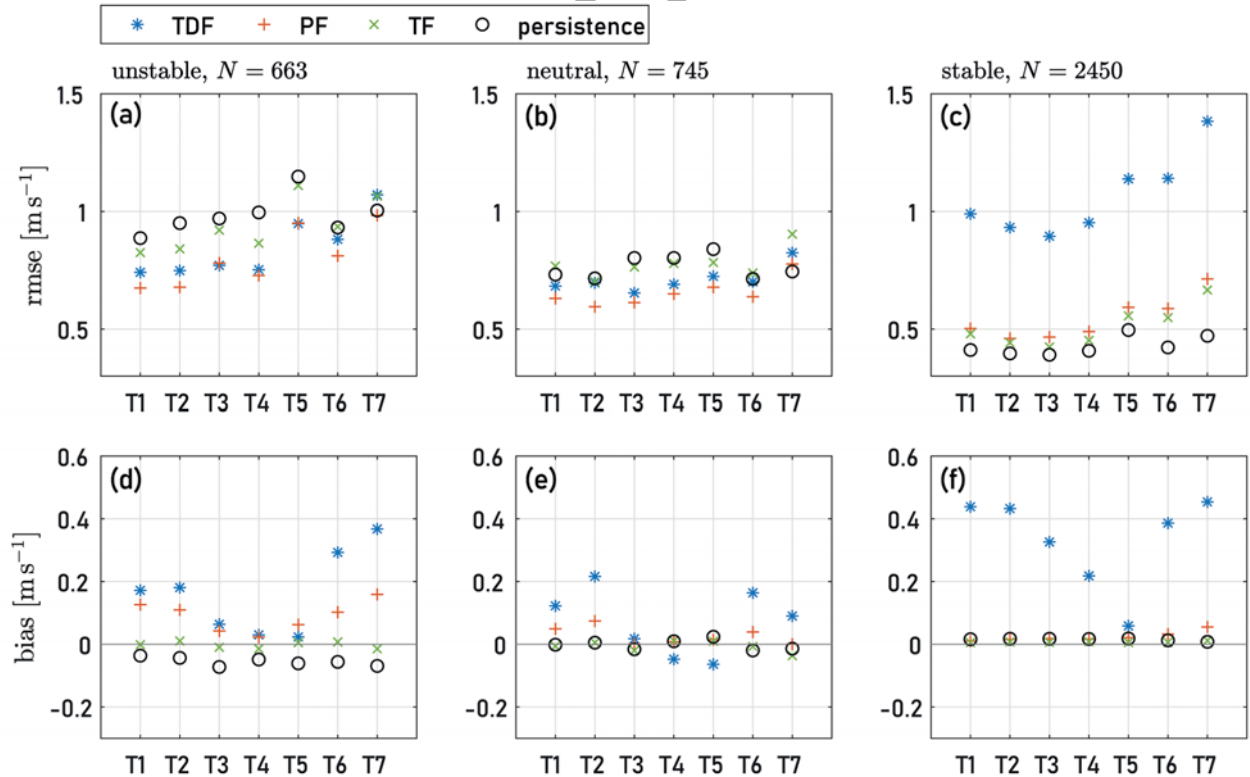


Figure 10: Forecast quality of the three lidar-based forecasts and persistence. The number of valid forecasts N , the rmse and bias of the different 5-minute ahead wind speed forecast for turbines T1–T7 and distinguishing between atmospheric stability are shown.

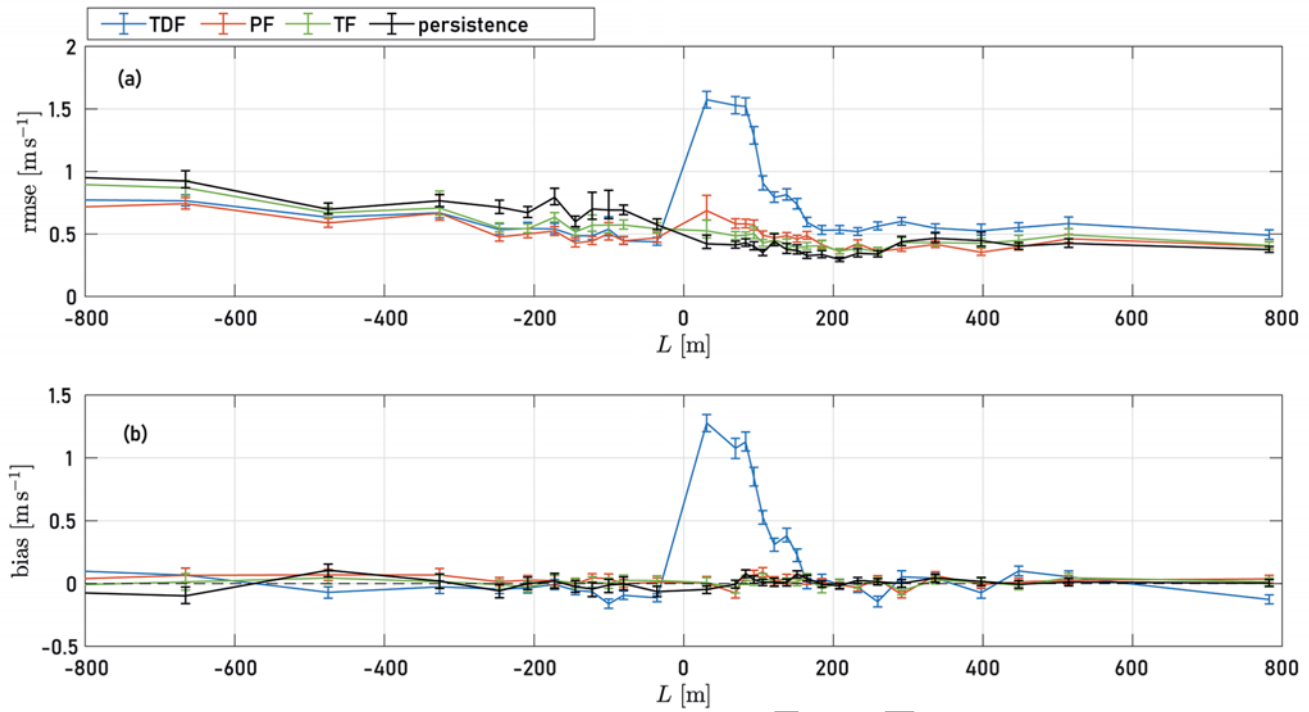


Figure 11: Forecast quality of the different 5-minute ahead wind speed forecasts dependent on Obukhov length L . In (a) the rmse and in (b) the bias are depicted. The 95 % confidence intervals are visualised as error bars. Each bin contains 716 values.

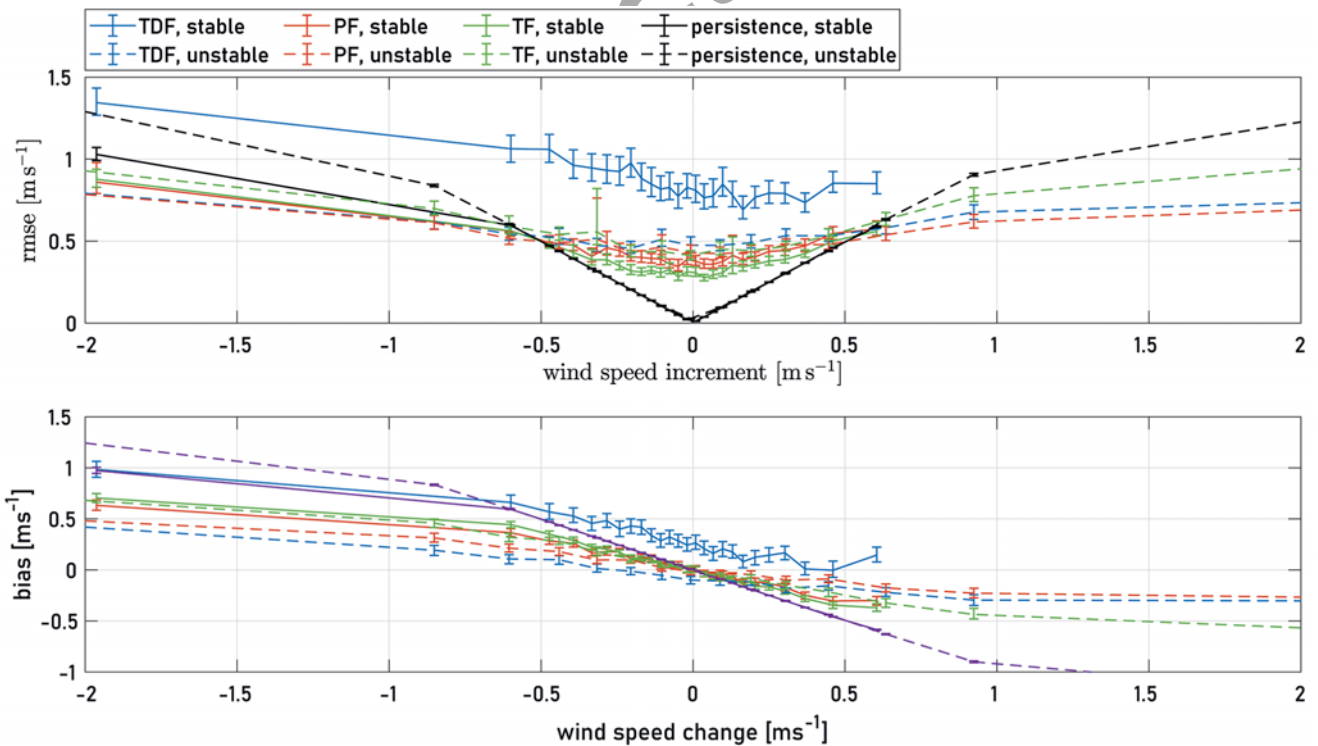


Figure 12: The rmse of the different 5-minute ahead wind speed forecasts dependent on 5-minute wind speed increments and distinguishing between stable and unstable situations. The 95 % confidence intervals are visualised as error bars. Stable cases contain 503 values per bin, unstable cases 574 values.

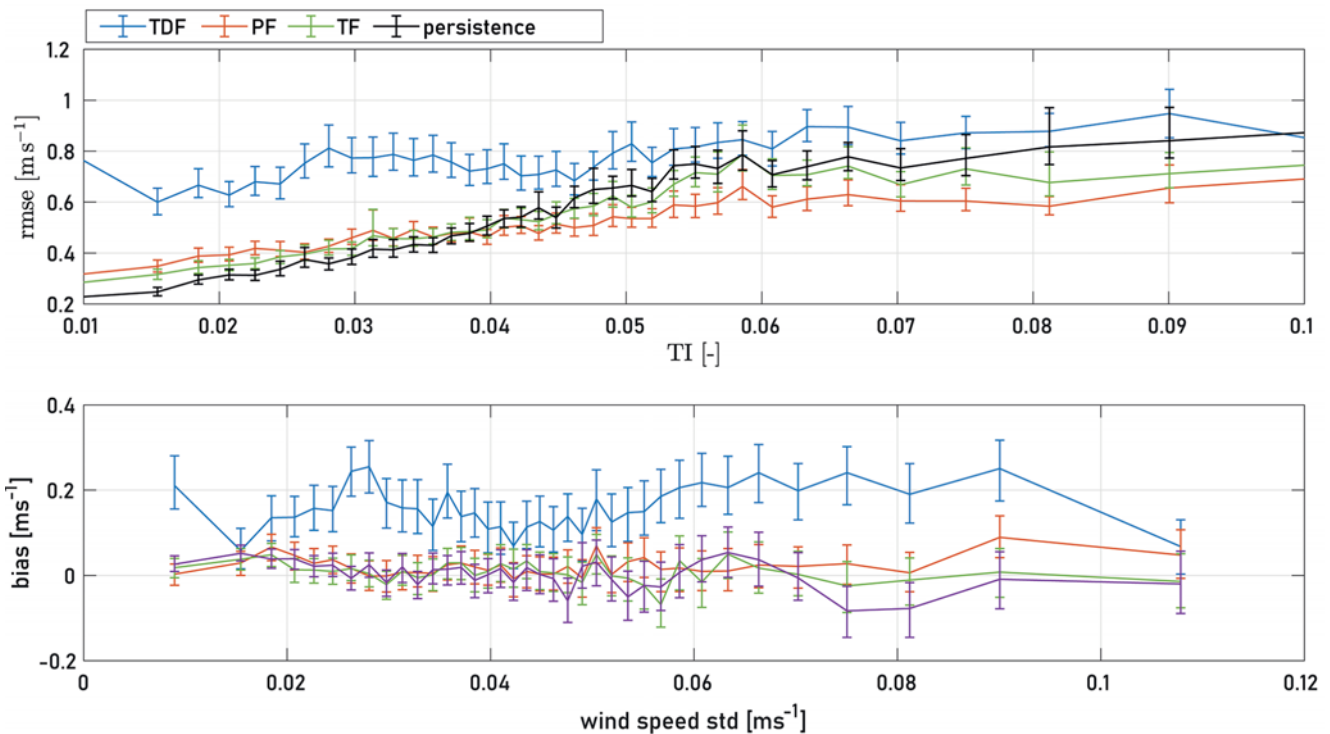


Figure 13: The rmse of the 5-minute ahead wind speed forecast dependent on the turbulence intensity TI. TI is computed from wind measurements observed up to 30 minutes prior to the forecast. The 95 % confidence intervals are visualised as error bars. Each bin contains 604 values.

Figure 13 visualises the rmse dependent on the normalised standard deviation of SCADA wind speed, i.e. turbulence intensity TI, computed using wind measurements observed up to 30 minutes prior to the forecast initialisation. Each bin contains 604 values. The rmse increases linearly with TI. Persistence shows the highest accuracy of all forecasts for $TI < 0.04$. However, the increase of rmse, i.e. the slope of the depicted curves, is smaller for TDF, PF and TF, indicating that the accuracy of these approaches is less sensitive to turbulence intensity. While the TDF has a generally larger error than the other approaches, the PF and TF can outperform persistence for a turbulence intensity above 0.04. Such situations were observed in 58 % of all analysed situations. The confidence intervals suggest that this result can be considered statistically significant for the PF, however, not for the TF.

5 Discussion

Here, we will first discuss the uncertainties related to the two methods for wind speed profile estimation TDF and PF. Further, implications for minute-scale forecasting are evaluated and the value of the newly introduced approaches is discussed.

5.1 Accuracy of vertical wind speed profile estimation

Our analysis has revealed the impact of individual input parameters on the accuracy of stability estimation and

consequently hub height wind speed. Temperature and wind speed measurement uncertainties have a strong influence on the accuracy of a stability parameter. Their effect on extrapolation accuracy is dominated by the influence of the stability correction term Ψ on the extrapolated wind speed. That means, as Ψ has such a large impact on u_{hh} in very stable situations, we expect larger uncertainties in wind speed extrapolation for those cases. This follows from the definition of the stability correction term and is true regardless of the exemplary uncertainties of the input parameters defined in Table 1. In a similar study, SAINT-DRENAN et al. (2009) found that already small uncertainties in temperature estimation result in considerable uncertainty in the shear estimation and consequently the extrapolated wind speed, particularly during very stable situations. For future applications, the installation of accurate temperature sensors is encouraged to enhance the stability estimation.

KELLY and JØRGENSEN (2017) discovered that the impact of misestimations of z_0 on wind resource estimation is minimal for small z_0 . For offshore situations with typical values in the order of $z_0 = 10^{-4}$ m, the estimated hub height wind speed is thus expected not to be influenced significantly by misestimations of roughness. Conclusively, determining z_0 by means of measured wind speed and L is considered a fair method for offshore wind speed forecasting.

Even though the uncertainty in measurement height estimation is small compared to that of stability and wind speed, especially in stable situations, it can con-

siderably impact the wind speed extrapolation accuracy. With increasing range gate, the lidar devices inclination will cause increasingly large deviations in the measuring height. Thus, especially for long-range lidar measurements, as used for minute-scale forecasting, the lidar alignment is of large importance (THEUER et al., 2020b). SCHNEEMANN et al. (2021) conducted a detailed uncertainty assessment of long-range lidar measurements and made recommendations for their offshore operation.

In addition to uncertainties of input parameters, one needs to consider that the stability-corrected logarithmic wind profile is not always a good representation of the true wind profile (KALVERLA et al., 2017). It is not possible to represent, for instance, kinks or reversed profiles. Especially during stable conditions, such profiles can be observed frequently (MØLLER et al., 2020). During such conditions, when wind speeds are described as strongly increasing by logarithmic profiles, the deviations between extrapolated and true profiles are considerable (THEUER et al., 2020b; MØLLER et al., 2020). Further, also the model describing the relation between the bulk Richardson number and the Obukhov length L (GRACHEV and FAIRALL, 1997) is subject to some inherent uncertainty that was not included in our analysis. Moreover, the assumptions based on the Monin–Obukhov similarity theory (MOST) are only valid in the surface layer. For larger altitudes the wind speed profile is increasingly affected by other parameters such as the boundary-layer depth (PEÑA et al., 2008). This might pose a problem in particular during very stable situations, when the surface layer is very shallow, thus possibly below the height of interest for large offshore wind turbines. However, also during neutral and unstable situations the atmospheric boundary layer height might have a non-negligible influence on the wind speed profile at hub height. In good agreement with the strongly positive bias of the TDF observed in this work (Section 4.3.3), several studies (PEÑA et al., 2008; OPTIS et al., 2014) have shown the logarithmic profiles tendency to overestimate wind speeds in high altitudes and during stable conditions. An analysis of another data set from this campaign by THEUER et al. (2020b) indicates that such situations start to occur with target heights of 61 m and extrapolation distances δz larger than 25 m and can thus be expected to impact wind speed extrapolation to the hub height of 92 m considered in this case. Future investigations could assess whether the use of a wind speed extrapolation method that takes into consideration the boundary layer depth and is valid beyond the surface layer (PEÑA et al., 2008; GRYNING et al., 2007; OPTIS et al., 2021) could improve wind speed extrapolation and the forecast skill of the TDF.

Taking into account the results of our study, a better alternative to wind speed extrapolation with the logarithmic profile is needed. Most beneficial for that purpose would be high-frequency wind profile measurements, e.g. lidar wind profiler measurements. However, in most cases such data is not available and one is restricted to the use of on-site meteorological measure-

ments. As an alternative, the profile fit approach utilises wind turbine operational data, which allows to better describe the wind shear from measuring to hub height. Particularly interesting are situations classified as very unstable and with comparably large fitted value of z_0 . In these cases, L is restricted by the decreasing wind speed with height. That means the main parameter to adjust the wind speed is the roughness length z_0 . On average, it was observed that z_0 increases by a factor of 4.5 compared to the originally calculated values. This factor is defined by the original value of L and the wind speed difference at hub height. It should be noted that the parameters determined by the profile fit cannot be understood as an accurate description of the atmospheric stability and roughness length, respectively, but rather describe the observed wind shear empirically.

5.2 Relevance for minute-scale forecasting

The profile fit-based forecast has benefits, particularly during stable stratification. The additional consideration of SCADA wind speed and the fitting approach allow to adjust for systematic errors in propagated wind vectors, for instance, caused by measurement height misestimation or errors in LOS wind speed measurements. This was confirmed by the results of the Monte Carlo simulations. Nevertheless, uncertainties are introduced whenever profiles change during the forecast horizon, most likely during dusk and dawn, or when only few data is available during the respective time period. Also the advection of wind vectors is expected to introduce uncertainties, influencing the accuracy of the fit. In such cases, it might be more accurate to rely on the TDF stability values. Generally, we expect that the PF would benefit from more detailed profile information, i.e. wind speed measurements at additional heights. Another advantage of the profile fit is its independence of meteorological measurements.

The tendency-based forecast avoids vertical profile extrapolation by considering two observed consecutive profiles. Also the consideration of recent SCADA data has a significant impact on the forecast's accuracy. Here, less weight is put onto the propagated lidar measurements and additionally wind speed measurements at hub height are considered. Persistence shows that in many cases the last observation of wind speed can provide accurate estimates of the next observation, especially during stable atmospheric conditions. Further, the Monte Carlo simulations revealed that wind vector estimation and propagation errors have less impact as not their absolute value, but only their tendency is considered in the TF forecast. Our analysis has further shown the TF's dependency on the extrapolation distance. This is on one hand related to the wind speed increments associated to larger extrapolation distances, but might on the other hand also be caused by increasing uncertainties in height extrapolation (THEUER et al., 2020b). As extrapolation distances can be significantly reduced when eliminating the lidar's tilt, this emphasises the need for a proper

972 alignment of the device. Alternatively, a bias correction
 973 might be able to improve the TF's accuracy.

974 As expected, the benchmark persistence is much
 975 more skilful during stable compared to unstable situations.
 976 Also the two newly introduced lidar-based approaches show lower errors during stable situations.
 977 This is in good agreement with the assumption that
 978 the applied advection techniques are more accurate during
 979 stable cases. Here, the evolution of larger structures
 980 dominates the flow compared to small scale buoyancy
 981 effects. WÜRTH et al. (2018) found that small wind
 982 speed fluctuations do not persist when propagated across
 983 larger distances and thus the prediction of flow over
 984 complex terrain is challenging. Further, we expect that
 985 turbines positioned within the wind farm cannot be pre-
 986 dicted well using Lagrangian advection. A more detailed
 987 analysis of different propagation techniques is therefore
 988 essential.

989 For future applications, it is important to be able to
 990 estimate the accuracy of each approach during different
 991 situations. We have identified the variability of the wind,
 992 expressed in terms of atmospheric stability or turbulence
 993 intensity as a major influencing factor. The lidar-based
 994 forecasts, in particular the PF, were found to be less
 995 sensitive to these parameters compared to persistence.
 996 This is also true for the dependency of forecast accuracy
 997 on the magnitude of the wind speed increment. While
 998 this is advantageous for wind speed changes larger than
 999 approximately 0.5 m s^{-1} , it also means that it is virtually
 1000 impossible to outperform persistence in situations
 1001 where wind speeds are almost constant. However, these
 1002 findings suggest that lidar-based methodologies can be
 1003 especially beneficial during wind ramps. This is con-
 1004 firmed by a recent study of VALDECABRES et al. (2020),
 1005 who forecasted the power of individual and aggregated
 1006 wind turbines using dual Doppler radar data with an em-
 1007 phasis on the prediction of ramp events. Such situations
 1008 are especially important for grid stability and electricity
 1009 trading and typically not represented well by statistical
 1010 models (PICHIAULT et al., 2021). Further, one could ar-
 1011 gue that the lidar-based forecast will become more ac-
 1012 curate than persistence with increasing lead time, as this
 1013 would result in a higher amount of large wind speed in-
 1014 crements. WÜRTH et al. (2018), for instance, found that
 1015 the accuracy of lidar-based forecasts compared to per-
 1016 sistence improves when considering larger lead times.
 1017 Also, WÜRTH et al. (2019) suggest that the advantages
 1018 of minute-ahead forecasts compared to persistence in-
 1019 crease with forecast horizon. We could not prove this
 1020 hypothesis as the measurement set-up restricted us to
 1021 5-minute ahead forecasts (THEUER et al., 2020a).

1022 In future analysis, the accuracy of wind power fore-
 1023 casts based on the introduced methods needs to be eval-
 1024 uated. As the two newly introduced methods are directly
 1025 based on the SCADA wind speed, a careful calibration
 1026 of the power curve used to translate wind speed to power
 1027 is necessary for each of the analysed turbines. Also the
 1028 non-linearity of the power curve will impact the forecast
 1029 skill (THEUER et al., 2020a).

6 Conclusions

We developed two new lidar-based forecasting methodologies in this work, and evaluated them against an existing approach and persistence under varying atmospheric conditions at an offshore wind farm, aiming to reduce the associated errors. The two new approaches additionally utilise wind turbine operational data to improve wind speed extrapolation to hub height. We also assessed the methods uncertainty under varying atmospheric conditions using an analytical uncertainty estimation of wind speed extrapolation by means of a stability-corrected logarithmic wind profile and using Monte Carlo simulations, to also capture uncertainties related to the lidar data processing and wind vector propagation.

Our results revealed the high potential of the profile fit-based approach and the tendency-based approach compared to the previously introduced temperature difference-based approach, particularly during stable atmospheric conditions. These two new approaches could outperform persistence during unstable and neutral stratification for situations with turbulence intensity greater than 4 % and wind speed increments larger than 0.5 m s^{-1} to 0.6 m s^{-1} .

Monte Carlo simulations highlighted their lower sensitivity to inaccurate input parameters, for instance wind speed and stability estimates. An analytical uncertainty estimation of the height extrapolation by means of a stability-corrected logarithmic profile confirmed the temperature difference-based approach's high uncertainty during very stable conditions due to large uncertainties in the stability correction term. Despite the much lower errors of the profile fit-based approach and tendency-based approach compared to the temperature difference-based approach these two new methods could not outperform persistence during stable stratification.

An accurate alignment of the lidar device could further improve the two new approaches. Wind speed measurements at additional heights, e.g. with a profiling lidar, would be beneficial especially for the profile fit-based approach.

We conclude that the additional use of wind turbine operational data has a significant positive impact on the forecast accuracy of lidar-based forecasts. This is especially of interest when no wind profile measurements or meteorological measurements are available. Generally, lidar-based forecasts were found to be less sensitive to atmospheric conditions than persistence. The characterisation of the approaches' forecast skill under different atmospheric conditions can be valuable for decision-making processes.

Acknowledgments

We thank the German Federal Environmental Foundation (DBU) as this project receives funding within the scope of their PhD scholarship program (Grant Nr. 20018/582).

The lidar measurements and parts of the work were performed within the research projects OWP Control (Ref. Nr. 0324131A), WIMS-Cluster (Ref. Nr. 0324005) and WindRamp (Ref. Nr. 03EE3027A) funded by the German Federal Ministry for Economic Affairs and Energy on the basis of a decision by the German Bundestag.

We acknowledge the wind farm operator Global Tech I Offshore Wind GmbH for providing SCADA data and thank them for supporting our work. We acknowledge the Met Office for making the OSTIA data set available.

We thank JÖRGE SCHNEEMANN and STEPHAN STONE for conducting the measurement campaign and ANDREAS ROTT for characterising the lidar misalignment and supporting our uncertainty analysis.

Author contributions

FT conducted the main research and wrote the manuscript. MFvD contributed to the scientific discussion, the structure of the paper and its detailed review. LvB and MK supervised the work, contributed to the scientific discussion and the structure of the paper and thoroughly reviewed the manuscript.

References

- BECK, H., M. KÜHN, 2017: Dynamic Data Filtering of Long-Range Doppler LiDAR Wind Speed Measurements. – *Remote Sens.* **9**, 561, DOI: [10.3390/rs9060561](https://doi.org/10.3390/rs9060561).
- BECK, H., M. KÜHN, 2019: Temporal Up-Sampling of Planar Long-Range Doppler LiDAR Wind Speed Measurements Using Space-Time Conversion. – *Remote Sens.* **11**, 867, DOI: [10.3390/rs11070867](https://doi.org/10.3390/rs11070867).
- BROMM, M., A. ROTT, H. BECK, L. VOLLMER, G. STEINFELD, M. KÜHN, 2018: Field investigation on the influence of yaw misalignment on the propagation of wind turbine wakes. – *Wind Energy* **21**, 1011–1028, DOI: [10.1002/we.2210](https://doi.org/10.1002/we.2210).
- CALI, Ü., 2011: Grid and Market Integration of Large-Scale Wind Farms Using Advanced Wind Power Forecasting: Technical and Energy Economic Aspects. – *Renewable Energies and Energy Efficiency* **17**, Kassel University Press.
- CUMMING, G., 2009: Inference by eye: Reading the overlap of independent confidence intervals. – *Statistics in Medicine* **28**, 205–220, DOI: [10.1002/sim.3471](https://doi.org/10.1002/sim.3471).
- GENCEEL, M., Z. YUXIAN, H. AOQI, 2018: Performance comparison of ANNs model with VMD for short-term wind speed forecasting. – *IET Renewable Power Generation* **12**, 1424–1430, DOI: [10.1049/iet-rpg.2018.5203](https://doi.org/10.1049/iet-rpg.2018.5203).
- GOOD, S., E. FIEDLER, C. MAO, M.J. MARTIN, A. MAYCOCK, R. REID, J. ROBERTS-JONES, T. SEARLE, J. WATERS, J. WHILE, M. WORSFOLD, 2020: The Current Configuration of the OSTIA System for Operational Production of Foundation Sea Surface Temperature and Ice Concentration Analyses. – *Remote Sens.* **12**, 720, DOI: [10.3390/rs12040720](https://doi.org/10.3390/rs12040720).
- GRACHEV, A., C. FAIRALL, 1997: Dependence of the monin-obukhov stability parameter on the bulk richardson number over the ocean. – *J. Appl. Meteor.* **36**, 406–414, DOI: [10.1175/1520-0450\(1997\)036<0406:DOTMOS>2.0.CO;2](https://doi.org/10.1175/1520-0450(1997)036<0406:DOTMOS>2.0.CO;2).
- GRYNING, S.E., E. BATCHVAROVA, B. BRÜMMER, H. JØRGENSEN, S. LARSEN, 2007: On the extension of the wind profile over homogeneous terrain beyond the surface boundary layer. – *Bound.-Layer Meteor.* **124**, 251–268, DOI: [10.1007/s10546-007-9166-9](https://doi.org/10.1007/s10546-007-9166-9).
- KALVERLA, P.C., G.J. STEENEVELD, R.J. RONDA, A.A. HOLTSLAG, 2017: An observational climatology of anomalous wind events at offshore meteomast IJmuiden (North Sea). – *J. Wind Engineer. Indust. Aerodynam.* **165**, 86–99, DOI: [10.1016/j.jweia.2017.03.008](https://doi.org/10.1016/j.jweia.2017.03.008).
- KELLY, M., H.E. JØRGENSEN, 2017: Statistical characterization of roughness uncertainty and impact on wind resource estimation. – *Wind Energy Sci.* **2**, 189–209, DOI: [10.5194/wes-2-189-2017](https://doi.org/10.5194/wes-2-189-2017).
- LENZI, A., I. STEINSLAND, P. PINSON, 2018: Benefits of spatiotemporal modeling for short-term wind power forecasting at both individual and aggregated levels. – *Environmetrics* **29**, e2493DOI: [10.1002/env.2493](https://doi.org/10.1002/env.2493).
- LIANG, Z., J. LIANG, C. WANG, X. DONG, X. MIAO, 2016: Short-term wind power combined forecasting based on error forecast correction. – *Energy Convers. Manag.* **119**, 215–226, DOI: [10.1016/j.enconman.2016.04.036](https://doi.org/10.1016/j.enconman.2016.04.036).
- MØLLER, M., P. DOMAGALSKI, L.R. SÆTRAN, 2020: Comparing abnormalities in onshore and offshore vertical wind profiles. – *Wind Energy Sci.* **5**, 391–411, DOI: [10.5194/wes-5-391-2020](https://doi.org/10.5194/wes-5-391-2020).
- OPTIS, M., A. MONAHAN, F.C. BOSVELD, 2014: Moving Beyond Monin–Obukhov Similarity Theory in Modelling Wind-Speed Profiles in the Lower Atmospheric Boundary Layer under Stable Stratification. – *Bound.-Layer Meteor.* **153**, 497–514, DOI: [10.1007/s10546-014-9953-z](https://doi.org/10.1007/s10546-014-9953-z).
- OPTIS, M., N.B.M. DEBNATH, P. DOUBRAWA, 2021: New methods to improve the vertical extrapolation of near-surface offshore wind speeds. – *Wind Energy Sci.* **6**, 935–948, DOI: [10.5194/wes-6-935-2021](https://doi.org/10.5194/wes-6-935-2021).
- PEÑA, A., S.E. GRYNING, C.B. HASAGER, 2008: Measurements and Modelling of the Wind Speed Profile in the Marine Atmospheric Boundary Layer. – *Bound.-Layer Meteor.* **129**, 479–495, DOI: [10.1007/s10546-008-9323-9](https://doi.org/10.1007/s10546-008-9323-9).
- PICHIAULT, M., C. VINCENT, G. SKIDMORE, J. MONTY, 2021: Characterisation of intra-hourly wind power ramps at the wind farm scale and associated processes. – *Wind Energy Sci.* **6**, 131–147, DOI: [10.5194/wes-6-131-2021](https://doi.org/10.5194/wes-6-131-2021).
- ROTT, A., J. SCHNEEMANN, F. THEUER, J.J.T. QUINTERO, M. KÜHN, in review: Alignment of scanning lidars in offshore wind farms. – *Wind Energy Sci. Discuss.* DOI: [10.5194/wes-2021-62](https://doi.org/10.5194/wes-2021-62).
- SAINT-DRENAN, Y.M., S. HAGEMANN, B. LANGE, J. TAMBKE, 2009: Uncertainty in the vertical extrapolation of the wind speed due to the measurement accuracy of the temperature difference. – European Wind Energy Science Conference and Exhibition, Marseille, France
- SANZ RODRIGO, J., E. CANTERO, B. GARCÍA, F. BORBÓN, U. IRIGOYEN, S. LOZANO, P. FERNANDES, R. CHÁVEZ, 2015: Atmospheric stability assessment for the characterization of offshore wind condition. – *J. Phys. Conf. Ser.* **625**, 012044, DOI: [10.1088/1742-6596/625/1/012044](https://doi.org/10.1088/1742-6596/625/1/012044).
- SCHNEEMANN, J., F. THEUER, A. ROTT, M. DÖRENKÄMPER, M. KÜHN, 2021: Offshore wind farm global blockage measured with scanning lidar. – *Wind Energy Sci.* **6**, 521–538, DOI: [10.5194/wes-2020-124](https://doi.org/10.5194/wes-2020-124).
- SMITH, S.D., 1980: Wind Stress and Heat Flux over the Ocean in Gale Force Winds. – *J. Phys. Ocean.* **10**, 709–726, DOI: [10.1175/1520-0485\(1980\)010<0709:WSAHFO>2.0.CO;2](https://doi.org/10.1175/1520-0485(1980)010<0709:WSAHFO>2.0.CO;2).
- THEUER, F., M.F. VAN DOOREN, L. VON BREMEN, M. KÜHN, 2020a: Minute-scale power forecast of offshore wind turbines using single-Doppler long-range lidar measurements. – *Wind Energy Sci.* **5**, 1449–1468, DOI: [10.5194/wes-5-1449-2020](https://doi.org/10.5194/wes-5-1449-2020).

- 1210 THEUER, F., M.F. VAN DOOREN, L. VON BREMEN, M. KÜHN,
1211 2020b: On the accuracy of a logarithmic extrapolation
1212 of the wind speed measured by horizontal lidar
1213 scans. – *J. Phys. Conf. Ser.* **1618**, 032043, DOI: [10.1088/1742-6596/1618/3/032043](https://doi.org/10.1088/1742-6596/1618/3/032043).
1214
- 1215 TORRES, J., A. GARCÍA, M.D. BLAS, A.D. FRANCISCO, 2005:
1216 Forecast of hourly average wind speed with ARMA models
1217 in Navarre (Spain). – *Solar Energy* **79**, 65–77, DOI: [10.1016/j.solener.2004.09.013](https://doi.org/10.1016/j.solener.2004.09.013).
1218
- 1219 VALLDECABRES, L., N. NYGAARD, L. VERA-TUDELA, L. VON BREMEN,
1220 M. KÜHN, 2018a: On the Use of Dual-Doppler Radar
1221 Measurements for Very Short-Term Wind Power Forecasts. –
1222 *Remote Sens.* **10**, 1701, DOI: [10.3390/rs10111701](https://doi.org/10.3390/rs10111701).
1223
- 1224 VALLDECABRES, L., A. PEÑA, M. COURTNEY, L. VON BREMEN,
1225 M. KÜHN, 2018b: Very short-term forecast of near-coastal
1226 flow using scanning lidars. – *Wind Energy Sci.* **3**, 313–327,
1227 DOI: [10.5194/wes-3-313-2018](https://doi.org/10.5194/wes-3-313-2018).
1228
- 1229 VALLDECABRES, L., L. VON BREMEN, M. KÜHN, 2020: Minute-
1230 Scale Detection and Probabilistic Prediction of Offshore Wind
Turbine Power Ramps using Dual-Doppler Radar. – *Wind
Energy* **23**, 1–23, DOI: [10.1002/we.2553](https://doi.org/10.1002/we.2553).
- 1231 WERNER, C., 2005: Lidar: Range-Resolved Optical Remote
1232 Sensing of the Atmosphere, chapter 12 – Doppler Wind Li-
1233 dar. – Springer New York, New York, NY, 325–354, DOI:
1234 [10.1007/0-387-25101-4_12](https://doi.org/10.1007/0-387-25101-4_12).
1235
- WÜRTH, I., S. ELLINGHAUS, M. WIGGER, M. J. NIEMEIER,
1236 A. CLIFTON, P. W CHENG, 2018: Forecasting wind ramps:
1237 can long-range lidar increase accuracy?. – *J. Phys. Conf. Ser.*
1238 **1102**, 012013, DOI: [10.1088/1742-6596/1102/1/012013](https://doi.org/10.1088/1742-6596/1102/1/012013).
1239
- WÜRTH, I., L. VALLDECABRES, E. SIMON, C. MÖHRLEN,
1240 B. UZUNOLU, C. GILBERT, G. GIEBEL, D. SCHLIPP,
1241 A. KAIFEL, 2019: Minute-Scale Forecasting of Wind
1242 Power–Results from the Collaborative Workshop of IEA
1243 Wind Task 32 and 36. – *Energies* **12**, 712, DOI: [10.3390/en12040712](https://doi.org/10.3390/en12040712).
1244
- ZHAO, J., Y. DUAN, X. LIU, 2018: Uncertainty Analysis of
1245 Weather Forecast Data for Cooling Load Forecasting Based on
1246 the Monte Carlo Method. – *Energies* **11**, 1900, DOI: [10.3390/en11071900](https://doi.org/10.3390/en11071900).
1247
- ZHOU, J., X. YU, B. JIN, 2018: Short-Term Wind Power Fore-
1248 casting: A New Hybrid Model Combined Extreme-Point Sym-
1249 metric Mode Decomposition, Extreme Learning Machine and
1250 Particle Swarm Optimization. – *Sustainability* **10**, 3202, DOI:
1251 [10.3390/su10093202](https://doi.org/10.3390/su10093202).
1252
- 1253